

First-principles study of disordered half-Heusler alloys $X\text{Fe}_{0.5}\text{Ni}_{0.5}\text{Sn}$ ($X = \text{Nb}, \text{Ta}$) as thermoelectric prospects

Mohd Zeeshan,¹ Chandan Kumar Vishwakarma,¹ and B. K. Mani^{1,*}

¹*Department of Physics, Indian Institute of Technology, Hauz Khas, New Delhi 110016, India*

(Dated: June 27, 2023)

High lattice thermal conductivity in half-Heusler alloys has been the major bottleneck in thermoelectric applications. Disordered half-Heusler alloys could be a plausible alternative to this predicament. In this paper, utilizing first-principles simulations, we have demonstrated the low lattice thermal conductivity in two such phases, $\text{NbFe}_{0.5}\text{Ni}_{0.5}\text{Sn}$ and $\text{TaFe}_{0.5}\text{Ni}_{0.5}\text{Sn}$, in comparison to well-known half-Heusler alloy TiCoSb . We trace the low thermal conductivity to their short phonon lifetime, originating from the interaction among acoustic and low-lying optical phonons. We recommend nanostructuring as an effective route in further diminishing the lattice thermal conductivity. We further predict that these alloys can be best used in the temperature range 400-600 K and carrier concentration of less than 10^{21} carriers cm^{-3} . We found $\sim 35\%$ and $\sim 17\%$ enhancement in ZT for $\text{NbFe}_{0.5}\text{Ni}_{0.5}\text{Sn}$ and $\text{TaFe}_{0.5}\text{Ni}_{0.5}\text{Sn}$, respectively, as compared to TiCoSb . We are optimistic of the findings and believe these materials would attract experimental investigations.

I. INTRODUCTION

Thermoelectric materials are best known for their virtuosity to directly convert waste heat into electricity [1]. The figure of merit of such materials is expressed as $ZT = S^2\sigma T/\kappa$, where S is the Seebeck coefficient, σ is the electrical conductivity, and $\kappa (= \kappa_e + \kappa_l)$ is the thermal conductivity comprising the electronic and lattice parts [2]. Half-Heusler (hH) alloys have garnered a tremendous reputation as potential thermoelectric candidates in the past two decades owing to their robust properties such as thermal stability [3], mechanical strength [4], non-toxic elements [5], semiconducting nature of 18-valence electron count (VEC) compositions [6], and tunable band gaps [7]. These alloys exhibit magnificent electrical transport properties on account of multiple band valleys and band degeneracy [8]. A record room temperature high power factor ($S^2\sigma$) of $106 \mu\text{W cm}^{-1} \text{K}^{-2}$ is reported in this family in the case of p -type $\text{Nb}_{0.95}\text{Ti}_{0.05}\text{FeSb}$ [9]. Albeit, the high lattice thermal conductivity originating from the relatively simple crystal structure of hH alloys overshadows their excellent electrical transport properties [10]. This is the foremost hurdle in maximizing the thermoelectric efficiency of hH alloys [11]. It is well-known that complex crystal structures having a large number of atoms exhibit remarkably low lattice thermal conductivity due to low velocity optical phonons [12].

Recently, based on similar guidelines, Anand *et al.* devised a rather unique valence-balanced approach for minimizing the lattice thermal conductivity in hH alloys [13]. The ordered composition TiCoSb was manipulated by replacing Co with 50% Fe and 50% Ni to arrive at the disordered composition $\text{TiFe}_{0.5}\text{Ni}_{0.5}\text{Sb}$. This way the 18-VEC is preserved and a relatively complex crystal structure is obtained which could have low intrinsic lattice thermal conductivity. To validate the point, $\text{TiFe}_{0.5}\text{Ni}_{0.5}\text{Sb}$

was synthesized and demonstrated to have almost three-fold lower room temperature lattice thermal conductivity than the parent composition TiCoSb . This highlights the significance of the approach and suggests that such disordered compositions could be preferred starting crystal structures in the search of low lattice thermal conductivity in hH alloys. The research in such disordered hH alloys is relatively new and is still in a growing phase. Interestingly, Anand *et al.* [13] have computationally shown that a much larger phase space is possible for exploration.

Thus, immediate experimental investigations would interest the thermoelectrics community. Though, experiments without any theoretical inputs could be challenging. Theoretical Insights into the electronic structure, understanding of electrical and thermal transport, favorable dopants to improve the transport properties, and a comprehensive estimate of the figure of merit would greatly facilitate the experimental realization. With this as motivation, we select two parent hH alloys NbCoSn and TaCoSn to make disordered compositions in the search of low intrinsic lattice thermal conductivity. We selected cobalt-based compositions because cobalt reserves are surmised as critical due to their extensive usage and it would be beneficial to replace Co with earth-abundant elements [14]. Thus, we replace Co with 50% Fe and 50% Ni in NbCoSn and TaCoSn to arrive at $\text{NbFe}_{0.5}\text{Ni}_{0.5}\text{Sn}$ and $\text{TaFe}_{0.5}\text{Ni}_{0.5}\text{Sn}$, respectively.

In this paper, utilizing the first-principles simulations, we have explored the thermoelectric potential of disordered hH alloys $\text{NbFe}_{0.5}\text{Ni}_{0.5}\text{Sn}$ (NFNS) and $\text{TaFe}_{0.5}\text{Ni}_{0.5}\text{Sn}$ (TFNS). Throughout this paper, we have used the well-known thermoelectric material TiCoSb of hH family as a reference to compare our results. Specifically, we have tried to address the following questions: i) Can the proposed alloys offer a lower lattice thermal conductivity than TiCoSb ? If yes, what could be the origin of such reduction? ii) What would be the impact on electronic structure and transport properties on re-

* bkmani@physics.iitd.ac.in

placing cobalt with iron and nickel, iii) And finally, can these disordered hH alloys lead to an enhanced figure of merit. If yes, at what temperature and carrier concentration range.

The paper is organized as follows: In Sec. II, we have provided a brief description of the computational methods employed in the calculations. In Sec. III, we present and discuss our results on electrical and thermal transport properties and based on that we estimate the figure of merit for the proposed disordered hH alloys. And finally, the summary of the paper is presented in Sec. IV.

Throughout this paper, we have used TiCoSb as a reference to compare our calculated results. This is because TiCoSb is a well-known thermoelectric material in hH family. For convenience, we call $\text{NbFe}_{0.5}\text{Ni}_{0.5}\text{Sn}$ and $\text{TaFe}_{0.5}\text{Ni}_{0.5}\text{Sn}$ as NFNS and TFNS, respectively.

II. COMPUTATIONAL METHODOLOGY

We performed the density functional theory based first-principles simulations using Vienna *ab initio* simulation package (VASP) [15, 16] to examine the thermoelectric prospects of TiCoSb, NFNS and TFNS systems. The generalized-gradient approximation based Perdew-Burke-Ernzerhof (PBE) [17] pseudopotential was employed to account for the exchange-correlation among electrons. The plane wave bases with an energy cutoff of 500 eV were used in all the calculations. Crystal structures were optimized using full relaxation calculations with the help of conjugate gradient algorithm using Monkhorst-Pack k -mesh of $11 \times 11 \times 11$. An energy convergence criterion of 10^{-8} eV was used for all self-consistent-field (SCF) calculations, and atomic forces were optimized up to 10^{-7} eV/Å. The SCF calculations for energy were carried out using a denser k -mesh of $21 \times 21 \times 21$.

Phonon dispersions and lattice thermal conductivity were computed using a $2 \times 2 \times 2$ (96 atoms) supercell. For phonons, we used the finite displacement approach as implemented in PHONOPY [18]. Force constants were calculated using the atomic displacement of 0.01 Å and Γ -centered k -mesh of $2 \times 2 \times 2$. For lattice thermal conductivity, the second- and third-order force constants were computed using the atomic displacements of 0.03 Å. We evaluated 2726 displacements to extract the third-order force constants. The lattice thermal conductivity was obtained by solving the linearized phonon Boltzmann transport equation within the single-mode relaxation time approximation as implemented in PHONO3PY [19]. The values of lattice thermal conductivity were tested for convergence with respect to q -mesh size and it was found to converge well with the q -mesh of $21 \times 21 \times 21$.

Electron lifetimes and electrical transport coefficients were obtained by solving the Boltzmann transport equation as implemented in AMSET [20]. We tested the convergence of transport properties with respect to increasing k -grid. We found that augmenting k -grid beyond

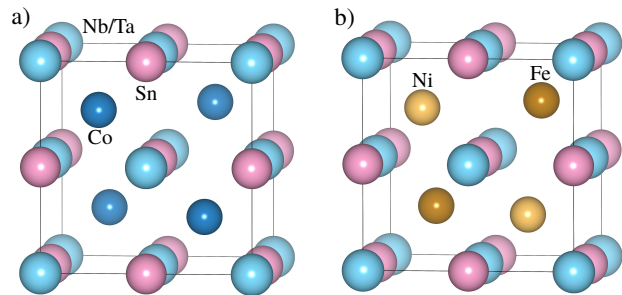


Figure 1. Crystal structure of (a) $X\text{CoSn}$ and (b) $X\text{Fe}_{0.5}\text{Ni}_{0.5}\text{Sn}$, where $X = \text{Nb/Ta}$. The structures are produced by using VESTA [21].

$21 \times 21 \times 21$ has negligible change in the transport properties. Further, the transport properties were tested for the convergence in terms of interpolation factor. A default interpolation factor of 10 lead to the converged transport properties.

III. RESULTS AND DISCUSSION

A. Crystal Structure and Phonon Dispersions

The crystal structure of hH alloys, XYZ , exists in $F\bar{4}3m$ symmetry, where X and Z form the zinc-blende type sublattice and Y -atoms occupy half of the tetrahedral voids [22]. To arrive at the aforementioned compositions of the disordered alloys, we replaced Co in $X\text{CoSn}$ ($X = \text{Nb, Ta}$) with 50% Fe and 50% Ni. Since all the tetrahedral voids positions are invariant under $F\bar{4}3m$ symmetry, the Fe/Ni can be introduced at any position. Thuswise, we obtained $\text{NbFe}_{0.5}\text{Ni}_{0.5}\text{Sn}$ and $\text{TaFe}_{0.5}\text{Ni}_{0.5}\text{Sn}$ structures, as shown in Fig. 1. However, the symmetry of these structures is expectedly reduces from $F\bar{4}3m$ to $P\bar{4}m2$. For optimization, we allowed all key degrees freedoms such as atomic positions, cell shape, and cell volume to relax, leading to an accurate ground state crystal structure. The optimized parameters for parent crystal structure, TiCoSb, are listed in Table I. We obtained a quite good agreement with the reported experimental and theoretical data. The calculated and experimental lattice constants [23] are consistent whereas the calculated band gap is in fairly good agreement with previous calculations [24–26]. The deviation of the calculated band gap from the experimental value could be attributed to the non-stoichiometric composition and antisite disordering as suggested by Sekimoto *et al* [27]. Nonetheless, it is important to note that the band gap survives on going from $X\text{CoSn}$ to $X\text{Fe}_{0.5}\text{Ni}_{0.5}\text{Sn}$ ($X = \text{Nb, Ta}$), which is a good indication for a thermoelectric material.

Using the optimized ground state structure, we computed the phonon dispersions by solving the eigenvalue

Table I. Cell parameters and band gaps from our calculations. The experimental and theoretical values are mentioned in parentheses and square brackets, respectively.

System	a (Å)	c (Å)	E_g (eV)
TiCoSb	5.88 (5.88)		1.05 (0.19) [23] [1.06] [24] [1.06] [25]
NbFe _{0.5} Ni _{0.5} Sn	5.97	6.00	0.10
TaFe _{0.5} Ni _{0.5} Sn	5.97	5.99	0.16
Wyckoff Positions			
Ti	0.00	0.00	0.00
Co	0.25	0.25	0.25
Sb	0.50	0.50	0.50
Nb/Ta	0.00	0.00	0.98
Fe	0.25	0.25	0.75
Ni	0.25	0.25	0.25
Sn	0.50	0.50	0.49

equation (as implemented in the Phonopy [18])

$$\sum_{\beta\tau'} D_{\tau\tau'}^{\alpha\beta}(\mathbf{q})\gamma_{\mathbf{q}j}^{\beta\tau'} = \omega_{\mathbf{q}j}^2\gamma_{\mathbf{q}j}^{\alpha\tau}. \quad (1)$$

Here, the indices τ, τ' represent the atoms, α, β are the Cartesian coordinates, \mathbf{q} is a wave vector and j is a band index. $D(\mathbf{q})$ refers to as the dynamical matrix, and ω and γ are the corresponding phonon frequency and polarization vector, respectively. Figure 2 shows the phonon dispersions for NFNS and TFNS, and the reference material TiCoSb. The absence of imaginary phonon frequencies suggests the dynamical stability of the proposed materials. Interestingly, these materials are also predicted to be thermodynamically stable [13]. Taken together, this greatly increases the likelihood of synthesis of NFNS and TFNS. Both NFNS and TFNS exhibit similar topology of phonons, which could be attributed to the same crystal structure. As to be expected, the phonon density of states show that the acoustic modes are predominantly occupied by the heavy atoms (Sb in TiCoSb, Sn in NFNS, and Ta in TFNS), high frequency optical modes by lighter atom Fe, and mid-frequency region collectively by the rest atoms.

As discernible from the figure, there is an apparent gap between the acoustic and optical (*a-o*) phonon modes for TiCoSb. Such a gap is often observed in hH alloys and is associated with their high lattice thermal conductivity [29]. Interestingly, this *a-o* gap disappears in NFNS and TFNS which opens up the possibility of phonon-phonon scattering among acoustic and low-lying optical modes. Thereby, the acoustic phonon modes, predominantly responsible for lattice thermal conductivity, are likely to

have a small lifetimes. To validate the same, we calculated the phonon lifetime at 300 K and the data from this is shown by the color bar in Fig. 2. Clearly, the phonon lifetime of NFNS and TFNS are shorter than that of TiCoSb, which hints at their low lattice thermal conductivity in comparison to TiCoSb. Thus, it will be interesting to examine the lattice thermal conductivity trend of the proposed materials.

B. Lattice Thermal Conductivity

Next we examine the lattice thermal conductivity, κ_L , for the proposed disordered alloys. κ_L is obtained by solving the linearized phonon Boltzmann transport equation as implemented in the PHONO3PY [19]. Figure 3(a) shows the calculated κ_L for NFNS, TFNS and the reference material TiCoSb. For comparison, we have also provided the experimental values for TiCoSb. We obtained slightly underestimated κ_L for TiCoSb in comparison to experimental values. It is to be, however, emphasized that the trend as function of temperature is same for both theory and experiment. The κ_L values of NFNS and TFNS bear close resemblance throughout the temperature range. The κ_L for TFNS is slightly higher than that of NFNS at 300 K, but later on the two data approach each other and the difference is negligible at 900 K. Interestingly, the κ_L of NFNS and TFNS is significantly lower than TiCoSb at 300 K, highlighting the importance of the substitution of Co with 50% Fe and Ni. Beyond 300 K, the difference in κ_L of the proposed materials and TiCoSb decreases. And, the reason for this could be attributed to the increasing phonon-phonon scattering with temperature. The smaller κ_L for NFNS and TFNS in comparison to TiCoSb could be attributed to their small phonon lifetimes, arising from the interaction among acoustic and low-lying optical modes. To gain further insight into the behavior of κ_L , we look into the phonon group velocities. As discernible from Figs. 4(a) - (c), the magnitude of group velocities is not significantly different in all three systems. This suggests that the phonon group velocities may not have played an important role in reducing the κ_L of the proposed materials.

Now we turn to understand the contribution of individual atoms to lattice thermal conductivity. For this, we calculated the cumulative κ_L as a function of phonon frequencies, shown in Figs. 4(d) - (f). The major contribution to κ_L is observed from the modes below 4 THz, around 81% in TiCoSb, 77% in NFNS, and 88% in TFNS. These modes are dominated by Sb in TiCoSb, Sn in NFNS, and Ta in TFNS. Thus, further reduction in κ_L may be facilitated by doping at Sn-site in NFNS, and Ta-site in TFNS. Further, we analyzed the cumulative κ_L with respect to phonon mean free path at 300 K and the data from this is shown in the, Fig. 3(b). As we observe from the figure, the phonons majorly contributing to κ_L have a mean free path in the range 0-50 nm in case of NFNS and TFNS. However, the mean free path

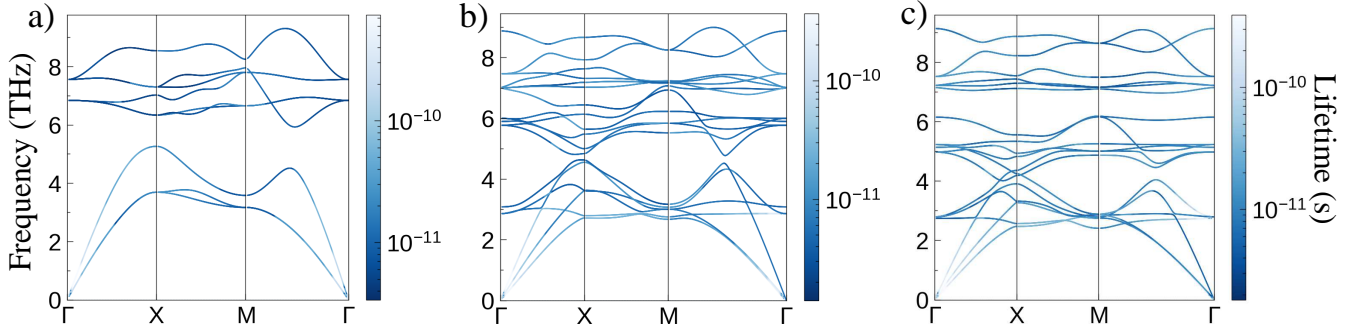


Figure 2. Calculated phonon dispersions of (a) TiCoSb, (b) NbFe_{0.5}Ni_{0.5}Sn, and (c) TaFe_{0.5}Ni_{0.5}Sn. The colorbar indicates the lifetime of ThermoPlotter [28].

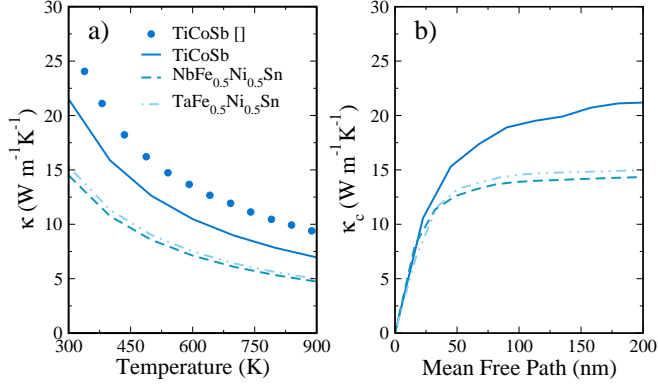


Figure 3. Calculated (a) average lattice thermal conductivity as a function of temperature and (b) cumulative lattice thermal conductivity as a function of phonon mean free path for TiCoSb, NbFe_{0.5}Ni_{0.5}Sn, and TaFe_{0.5}Ni_{0.5}Sn. The empty circles represent the experimental data for TiCoSb [23].

ranges up to 90 nm for phonons boosting κ_L in TiCoSb. This shows that the phonon mean free path of NFNS and TFNS are shorter as compared to TiCoSb, which is an indicative of low κ_L in NFNS/TFNS. This short mean free path is consistent with the small phonon lifetime of NFNS/TFNS, as discussed before. It is noteworthy that $\sim 15\%$ contribution to κ_L in NFNS/TFNS comes from the phonons with a mean free path larger than 50 nm. Thus, in our opinion, nanostructuring could be an effective strategy for further diminishing the κ_L for the proposed materials.

Altogether, we have demonstrated the low κ_L in disordered hH alloys NFNS and TFNS in comparison to well-known hH alloy TiCoSb. In the next section, we explore the electronic structure and electrical transport properties of the proposed materials.

C. Electronic Structure and Transport Properties

The calculated electronic band structures for NFNS, TFNS, and the reference material TiCoSb is shown in

Table II. Calculated figure of merit for TiCoSb, NbFe_{0.5}Ni_{0.5}Sn, and TaFe_{0.5}Ni_{0.5}Sn at different temperatures and carrier concentrations.

T (K)	n (cm ⁻³)	ZT		
		TiCoSb	NFNS	TFNS
300	1×10^{20}	0.05	0.09	0.08
400	2×10^{20}	0.09	0.14	0.12
500	3×10^{20}	0.13	0.18	0.16
600	4×10^{20}	0.17	0.23	0.20
700	5×10^{20}	0.21	0.25	0.23
800	6×10^{20}	0.24	0.25	0.26
900	7×10^{20}	0.26	0.26	0.26

Fig. 5. The electronic structure of TiCoSb is well explored in the literature [24–26]. Our computed data is consistent with the literature in terms of reported theoretical band gap of 1.06 eV [24, 25]. As mentioned earlier, both NFNS and TFNS are observed to be semiconducting. The nature of the band gap is direct at the Γ -position in the case of TiCoSb, whereas it is indirect ($A-\Gamma$) for both NFNS and TFNS. The band degeneracy, as observed in the case of TiCoSb, is a characteristic of exemplary electrical transport properties [30]. The valence band maximum (VBM) and conduction band minimum (CBM) are threefold degenerate in the case of TiCoSb. However, the degeneracy is reduced to twofold at VBM in NFNS and TFNS. Not only this, the band gap is drastically reduced to 0.1 eV. We trace this reduced band gap majorly to the states originating from Fe-atoms. This can be seen from the atom projected density of states given in the supplemental material [31]. The reduced band degeneracy and band gap are likely to affect the electrical transport properties. We anticipate a better Seebeck coefficient in TiCoSb on account of degenerate bands, whereas a better electrical conductivity in NFNS and TFNS because of the small band gap.

To get further insight into the transport properties,

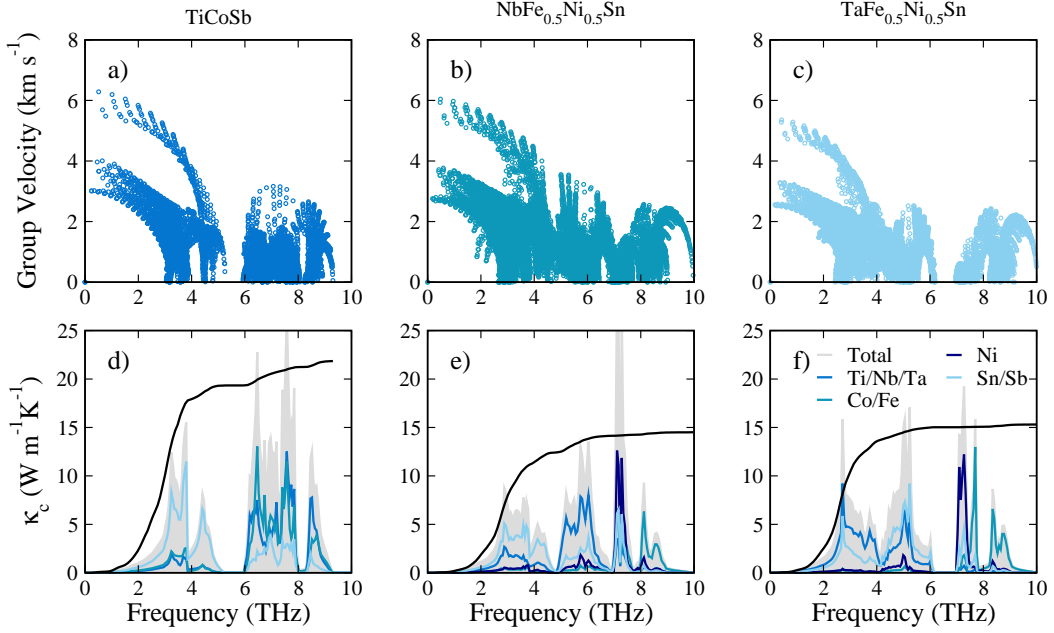


Figure 4. Calculated [(a), (b), and (c)] average phonon group velocities and [(d), (e), and (f)] cumulative lattice thermal

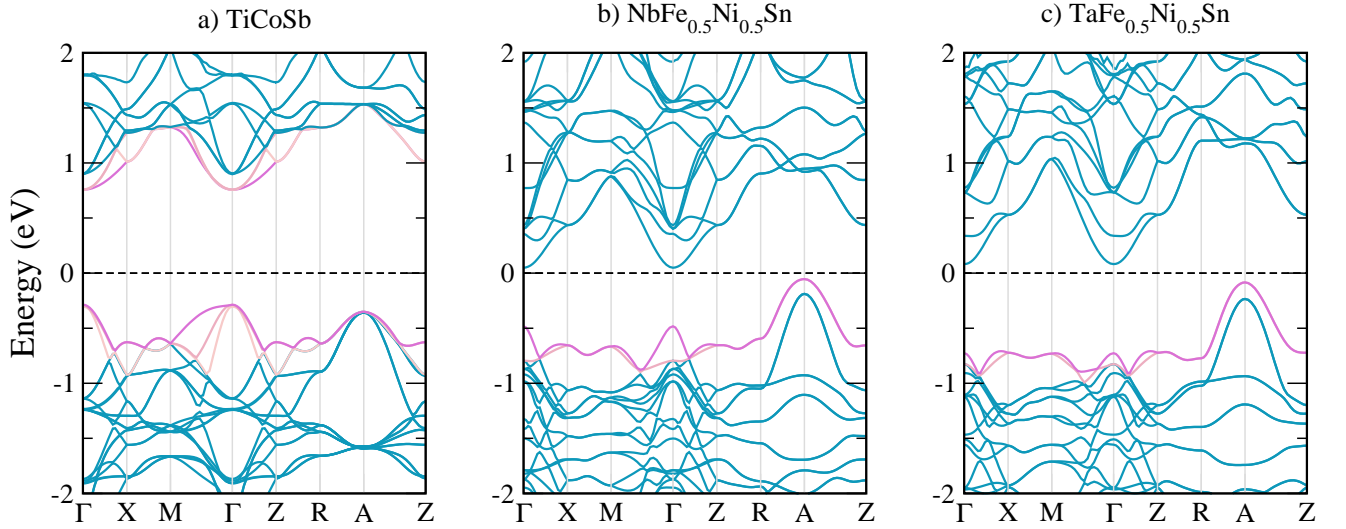


Figure 5. Calculated electronic band structures for (a) TiCoSb, (b) NbFe_{0.5}Ni_{0.5}Sn, and (c) TaFe_{0.5}Ni_{0.5}Sn. The degenerate bands at VBM and CBM are highlighted in different colors.

next we computed the electrical transport coefficients S , σ , and κ_e . These are derived from the generalized transport coefficient (as implemented in AMSET [20]), expressed as

$$\mathcal{L}_{\alpha\beta}^n = e^2 \int \sum_{\alpha\beta}(\varepsilon)(\varepsilon - \varepsilon_F)^n \left[-\frac{\partial f^0}{\partial \varepsilon} \right] d\varepsilon, \quad (2)$$

where ε_F is Fermi level at a particular doping, f^0 is the Fermi distribution function, and $\sum_{\alpha\beta}(\varepsilon)$ is the spectral conductivity. Since electrical transport parameters are susceptible to the charge carriers' relaxation time,

it is important to evaluate the scattering rate for accurately governing the transport properties. We obtained the same using scattering mechanisms such as acoustic deformation potential (ADP), ionized impurity (IMP), polar optical phonon (POP), and the piezoelectric (PZ) scattering. The various parameters computed for different scattering mechanisms include deformation potential, elastic constant, piezoelectric coefficient, polar optical phonon frequency, and static and high-frequency dielectric constants.

The calculated scattering rates at different tempera-

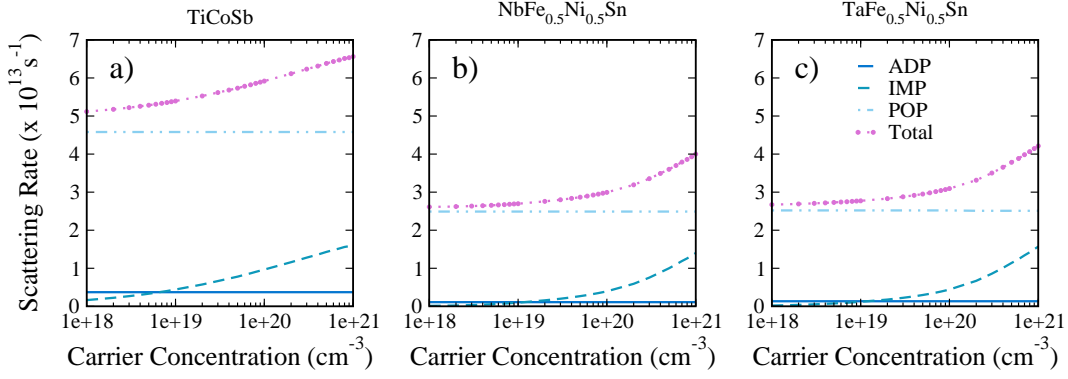


Figure 6. Calculated scattering rates at 300 K for *p*-type (a) TiCoSb, (b) NbFe_{0.5}Ni_{0.5}Sn, and (c) TaFe_{0.5}Ni_{0.5}Sn systems.

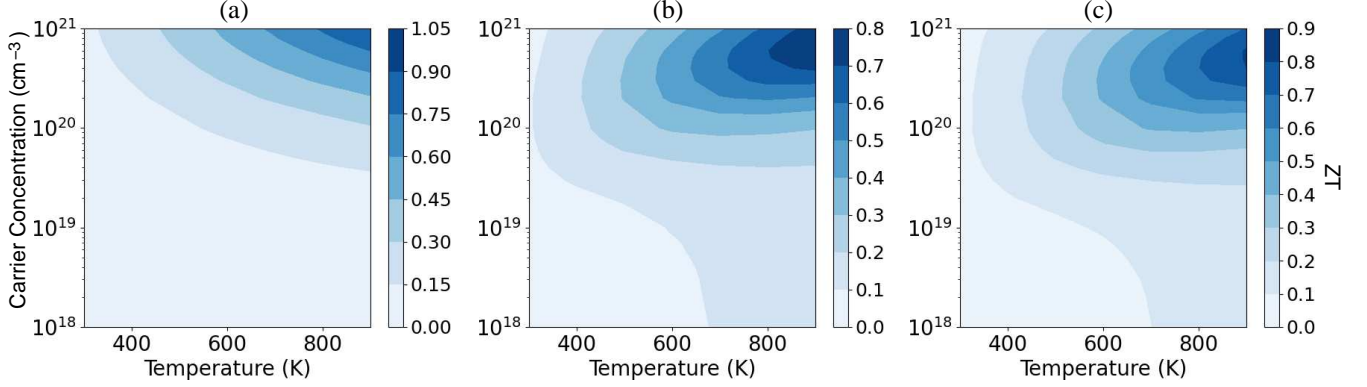


Figure 7. Calculated figure of merit as a function of temperature and carrier concentration for (a) TiCoSb, (b) NbFe_{0.5}Ni_{0.5}Sn,

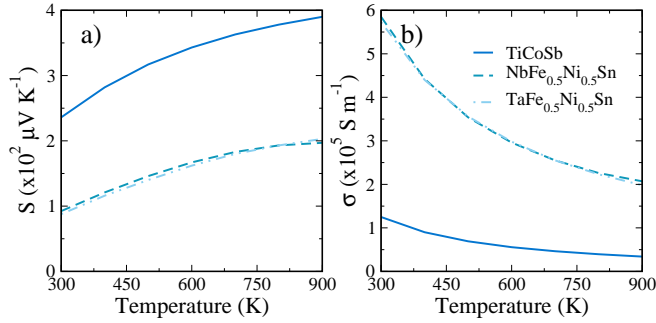


Figure 8. Calculated (a) Seebeck coefficient and (b) electrical conductivity as a function of temperature at 4×10^{20} carriers cm^{-3} for TiCoSb, NbFe_{0.5}Ni_{0.5}Sn, and TaFe_{0.5}Ni_{0.5}Sn systems.

tures and carrier concentrations are provided in the supplemental material [31]. Here, we have shown the calculated scattering rates at 300 K for TiCoSb, NFNS, and TFNS, Fig. 6. For clarity, we choose to show the results only for *p*-type carrier concentration. This is because we obtained significant results for *p*-type in comparison to *n*-type carrier concentration. Further, TiCoSb is well-known as a *p*-type thermoelectric material. Nonetheless, as discernible from the figure, the contribution of

ADP and POP scattering at 300 K remains constant throughout the considered range of carrier concentration. The IMP scattering however increases gradually and then gains upon ADP beyond carrier concentration of 10^{19} carriers cm^{-3} . The increase in IMP with increasing carrier concentration could be attributed to the increased ionized impurities. However, the dominant contribution is from POP in all the cases. The total scattering rate mirrors the trend of IMP scattering. Overall, at 300 K, the scattering rate ranges $5 - 6.5 \times 10^{13} \text{ s}^{-1}$ for TiCoSb and $2.6 - 4.2 \times 10^{13} \text{ s}^{-1}$ for NFNS and TFNS. Incorporating these scattering rates we computed the figure of merit and the data from this is shown in Fig. 7. It is to be however mentioned that, we have used κ_L of parent compositions for evaluating the figure of merit since it is computationally challenging to calculate κ_L at each carrier concentration.

The trend of the figure of merit is quite obvious from the trend of its components S , σ , and κ_e given in the supplemental material [31]. As to be expected, the S and σ show the opposite trends, i.e, S is maximum near low carrier concentrations, whereas σ exhibits higher values at high carrier concentrations. The S dominates in case of TiCoSb, whereas σ in NFNS and TFNS is almost four-fold higher in comparison to TiCoSb. This is consistent

with the observation made from the electronic structure. It is interesting to note that the power factor of all three systems is of the same order. The maximum power factor obtained is $105 \mu\text{W cm}^{-1} \text{K}^{-2}$. Thus, κ_e is quite crucial which is significantly high in NFNS and TFNS.

Taking all together, the highest figure of merit obtained are 1.0, 0.8, and 0.9, respectively, for TiCoSb, NFNS, and TFNS at 900 K and carrier concentration of 1×10^{21} carriers cm^{-3} . This suggest that the proposed alloys at high temperatures and high carrier concentration range are competitive with TiCoSb. At lower temperatures and lower concentrations, however, the proposed alloys show an edge over the parent TiCoSb. The figure of merit for TiCoSb is less than 0.15 up to 500 K in the carrier concentration range 1×10^{18} to 1×10^{20} carriers cm^{-3} . On the other hand, the ZT of NFNS and TFNS increases consistently with temperature and carrier concentration. As a matter of fact, NFNS and TFNS have improved ZT value than TiCoSb in the temperature region 300-700 K for the carrier concentration in the range 1×10^{18} – 5×10^{20} carriers cm^{-3} . As evident from the Table II, for a fixed carrier concentration of 4×10^{20} carriers cm^{-3} , at 600 K, the ZT for NFNS and TFNS are larger by $\sim 35\%$ and $\sim 17\%$, respectively, than TiCoSb. This shows that the proposed materials can be better thermoelectric prospects as compared to TiCoSb up to 600 K and carrier concentration less than 10^{21} carriers cm^{-3} . It should be emphasized that experimentally it is often more convenient to introduce a small carrier concentration. Thus, a better performance of NFNS and TFNS as compared to TiCoSb at smaller doping concentrations could be advantageous from experimental perspective. Additionally, the proposed values can be further improved by nanostructuring. Further, in Fig. 8 we have shown the variation of Seebeck coefficient and electrical conductivity with temperature for the carrier concentration of 4×10^{20} carriers cm^{-3} . As we observed from the figure, the Seebeck coefficient is dominant for TiCoSb and increases with temperature. The electrical conductivity, however, dominates in the case of NFNS/TFNS and shows an opposite trend of decreasing values with

temperature.

IV. CONCLUSION

In conclusion, utilizing first-principles simulations, we have explored the thermoelectric properties of two disordered half-Heusler alloys NbFe_{0.5}Ni_{0.5}Sn and TaFe_{0.5}Ni_{0.5}Sn. Both systems optimize in $P4m2$ symmetry and possess a band gap of 0.1 eV. The phonon dispersions indicate their dynamical stability. Interestingly, the characteristic gap in acoustic and optical phonons, which imparts high lattice thermal conductivity to half-Heusler alloys, disappears in both materials. Likewise, we obtained significantly low lattice thermal conductivity in NbFe_{0.5}Ni_{0.5}Sn and TaFe_{0.5}Ni_{0.5}Sn in comparison to TiCoSb. We attribute this change in thermal conductivity to the short phonon lifetime of NbFe_{0.5}Ni_{0.5}Sn and TaFe_{0.5}Ni_{0.5}Sn, arising from the interaction among acoustic and low-lying optical modes. Our simulations on lattice thermal conductivity with phonon mean free path suggest that, nanostructuring could bring down the lattice thermal conductivity further. Electrical transport results reveal that these materials are best suited in the temperature range 400–600 K and in the carrier concentration range less than 10^{21} carriers cm^{-3} . Within these temperature and concentration range, we find $\sim 35\%$ and $\sim 17\%$ enhancement in the ZT value for NbFe_{0.5}Ni_{0.5}Sn and TaFe_{0.5}Ni_{0.5}Sn, respectively, as compared to TiCoSb. We hope that our results would encourage experimental investigations in these proposed materials.

ACKNOWLEDGMENTS

M. Z. and C. K. V. are thankful to MHRD and CSIR, respectively, for their financial assistance. B. K. M. acknowledges the funding support from the SERB, DST (ECR/2016/001454). The calculations are performed using the High Performance Computing cluster, Padum, at the Indian Institute of Technology Delhi.

-
- [1] B. Jiang, Y. Yu, H. Chen, J. Cui, X. Liu, L. Xie, and J. He, *Nature Commun.* **12**, 3234 (2021).
 - [2] F. Garmroudi, A. Riss, M. Parzer, N. Reumann, H. Müller, E. Bauer, S. Khmelevskiy, R. Podloucky, T. Mori, K. Tobita, Y. Katsura, and K. Kimura, *Phys. Rev. B* **103**, 085202 (2021).
 - [3] A. Roy, J. W. Bennett, K. M. Rabe, and D. Vanderbilt, *Phys. Rev. Lett.* **109**, 037602 (2012).
 - [4] T. Berry, C. Fu, G. Auffermann, G. H. Fecher, W. Schnelle, F. Serrano-Sanchez, Y. Yue, H. Liang, and C. Felser, *Chem. Mater.* **29**, 7042 (2017).
 - [5] W. Li, G. Yang, and J. Zhang, *J. Phys. D: Appl. Phys.* **49**, 195601 (2016).
 - [6] M. Zeeshan, T. Nautiyal, J. van den Brink, and H. C. Kandpal, *Phys. Rev. Materials* **2**, 065407 (2018).
 - [7] I. Galanakis, P. H. Dederichs, and N. Papanikolaou, *Phys. Rev. B* **66**, 174429 (2002).
 - [8] J. Zhou, H. Zhu, T.-H. Liu, Q. Song, R. He, J. Mao, Z. Liu, W. Ren, B. Liao, D. J. Singh, Z. Ren, and G. Chen, *Nature Commun.* **9**, 1721 (2018).
 - [9] R. He, D. Kraemer, J. Mao, L. Zeng, Q. Jie, Y. Lan, C. Li, J. Shuai, H. S. Kim, Y. Liu, D. Broido, C.-W. Chu, G. Chen, and Z. Ren, *Proceedings of the National Academy of Sciences* **113**, 13576 (2016).
 - [10] S. Chen and Z. Ren, *Materials Today* **16**, 387 (2013).

- [11] W. Xie, A. Weidenkaff, X. Tang, Q. Zhang, J. Poon, and T. M. Tritt, *Nanomaterials* **2**, 379 (2012).
- [12] E. S. Toberer, A. Zevalkink, and G. J. Snyder, *J. Mater. Chem.* **21**, 15843 (2011).
- [13] S. Anand, M. Wood, Y. Xia, C. Wolverton, and G. J. Snyder, *Joule* **3**, 1226 (2019).
- [14] Z. Liu, S. Guo, Y. Wu, J. Mao, Q. Zhu, H. Zhu, Y. Pei, J. Sui, Y. Zhang, and Z. Ren, *Advanced Functional Materials* **29**, 1905044 (2019).
- [15] G. Kresse and J. Furthmüller, *Comput. Mater. Sci.* **6**, 15 (1996).
- [16] G. Kresse and J. Furthmüller, *Phys. Rev. B* **54**, 11169 (1996).
- [17] J. P. Perdew, K. Burke, and M. Ernzerhof, *Phys. Rev. Lett.* **77**, 3865 (1996).
- [18] A. Togo and I. Tanaka, *Scr. Mater.* **108**, 1 (2015).
- [19] A. Togo, L. Chaput, and I. Tanaka, *Phys. Rev. B* **91**, 094306 (2015).
- [20] A. M. Ganose, J. Park, A. Faghaninia, R. Woods-Robinson, K. A. Persson, and A. Jain, *Nature Commun.* **12**, 2222 (2021).
- [21] K. Momma and F. Izumi, *J. Appl. Crystallogr.* **44**, 1272 (2011).
- [22] F. Casper, C. Felser, R. Seshadri, C. P. Sebastian, and R. Pöttgen, *J. Phys. D: Appl. Phys.* **41**, 035002 (2008).
- [23] T. Sekimoto, K. Kurosaki, H. Muta, and S. Yamanaka, *Mater. Trans.* **47**, 1445 (2006).
- [24] B. Xu, J. Zhang, J. Liang, G. Gao, and L. Yi, *Journal of Solid State Chemistry* **192**, 351 (2012).
- [25] L. L. Wang, L. Miao, Z. Y. Wang, W. Wei, R. Xiong, H. J. Liu, J. Shi, and X. F. Tang, *Journal of Applied Physics* **105**, 013709 (2009), <https://doi.org/10.1063/1.3056384>.
- [26] M. Zeeshan, H. K. Singh, J. van den Brink, and H. C. Kandpal, *Phys. Rev. Mater.* **1**, 075407 (2017).
- [27] T. Sekimoto, K. Kurosaki, H. Muta, and S. Yamanaka, *International Conference on Thermoelectrics 2005* (IEEE, Piscataway, 2005).
- [28] K. B. Spooner, M. Einhorn, D. W. Davies, and D. O. Scanlon, *ThermoPlotter*, Online, <https://github.com/SMTG-UCL/ThermoPlotter> (2021).
- [29] X. Yu and J. Hong, *J. Mater. Chem. C* **9**, 12420 (2021).
- [30] Y. Tang, Z. M. Gibbs, L. A. Agapito, G. Li, H.-S. Kim, M. B. Nardelli, S. Curtarolo, and G. J. Snyder, *Nature Mater.* **14**, 1223 (2015).
- [31] See Supplemental Material at [URL].